

Observational Appearance of a Freely-falling Star in an Asymmetric Thin-shell Wormhole

Yiqian Chen^{a,*}, Peng Wang^{a,†}, Houwen Wu^{a,b,‡} and Haitang Yang^{a,§}

^a*Center for Theoretical Physics, College of Physics,
Sichuan University, Chengdu, 610064, China and*

^b*Department of Applied Mathematics and Theoretical Physics,
University of Cambridge, Wilberforce Road, Cambridge, CB3 0WA, UK*

It has been recently reported that, at late times, the total luminosity of a star freely falling in black holes decays exponentially with time, and one or two series of flashes with decreasing intensity are seen by a specific observer, depending on the number of photon spheres. In this paper, we examine observational appearances of an infalling star in a reflection-asymmetric wormhole, which has two photon spheres, one on each side of the wormhole. We find that the late-time total luminosity measured by distant observers gradually decays with time or remains roughly constant due to the absence of the event horizon. Moreover, a specific observer would detect a couple of light flashes in a bright background at late times. These observations would offer a new tool to distinguish wormholes from black holes, even those with multiple photon spheres.

arXiv:2210.10948v1 [gr-qc] 20 Oct 2022

* chenyiqian@stu.scu.edu.cn

† pengw@scu.edu.cn

‡ hw598@damtp.cam.ac.uk

§ hyanga@scu.edu.cn

CONTENTS

I. Introduction	2
II. Setup	4
III. Numerical Results	7
A. Scenario I	10
B. Scenario II	14
IV. Conclusions	18
Acknowledgments	20
References	20

I. INTRODUCTION

The Event Horizon Telescope (EHT) collaboration released images of the supermassive black holes M87* [1–8] and Sgr A* [9–14], which provides a new method to test general relativity in the strong field regime. The main feature displayed in these images is a central brightness depression, namely black hole shadow, surrounded by a bright ring. The edge of black hole shadow involves a critical curve in the sky of observers, which is closely related to some unstable bound photon orbits. For static spherically symmetric black holes, unstable photon orbits form photon spheres outside the event horizon. Since light rays undergo strong gravitational lensing near photon spheres, black hole images encode valuable information of the geometry in the vicinity of photon spheres. Therefore, black hole images have been widely studied in the context of different theories of gravity, e.g., nonlinear electrodynamics [15–21], the Gauss-Bonnet theory [22–25], the Chern-Simons type theory [26, 27], $f(R)$ gravity [28–30], string inspired black holes [31–34] and other theories [35–46].

On the other hand, testing the nature of compact objects in the universe has been an important question in astrophysics for decades. Although the black hole images captured by EHT are in good agreement with the predictions of Kerr black holes, the black hole mass/distance and EHT systematic uncertainties still leave some room within observational uncertainty bounds for black hole mimickers. Among all black hole mimickers, ultra compact objects (UCOs), e.g., boson stars, gravastars and wormholes, which are horizonless and possess light rings (or photon spheres in the spherically symmetric case), are of particular interest since their observational signatures

can be quite similar to those of black holes [47–50]. Nevertheless, it is of great importance to seek observational signals to distinguish UCOs from black holes. For example, due to a reflective surface or an extra photon sphere, echo signals associated with the post-merger ringdown phase in the binary black hole waveforms can be found in various ECO models [51–61]. In addition, asymmetric thin-shell wormholes with two photon spheres were found to have double shadows and an additional photon ring in their images [62–66]. For black holes with one photon sphere, there is one shadow and one photon ring in black hole images, and no echo signal in late-time waveforms. These observational features would allow us to distinguish wormholes from black holes with one photon sphere.

Intriguingly, more than one photon sphere has been reported to exist outside the event horizon for a class of hairy black holes in certain parameter regions [67–71]. Multiple photon spheres can introduce distinctive features in black hole images, e.g., double shadows [71], extra photon rings [72] and tripling higher-order images [73]. Furthermore, late-time echo signals were also observed since the effective potential of a scalar perturbation possesses a multiple-peak structure [74, 75].

Can we distinguish black holes with multiple photon spheres from UCOs? To answer this question, we investigate dynamic observations of a luminous object freely falling in an asymmetric thin-shell wormhole in this paper. Lately, observational appearances of a star freely falling onto black holes with a single or double photon spheres have been numerically simulated [76, 77]. Particularly, the total observed luminosity fades out exponentially with a declining tail, which is caused by photons orbiting around the photon sphere, in the single-photon-sphere case. In contrast, when there exist two photon spheres, the total luminosity exhibits two exponential decays and a sharp peak between them. In addition, due to photons trapped between two photon spheres, a specific observer can detect one more cascade of flashes in the double-photon-sphere case.

Recently, luminous matter falling onto a black hole has been reported to occur periodically near the Cyg X-1 [78] and the Sgr A* source [79, 80]. Moreover, a new way to measure the spin of Sgr A* was proposed by simulating an infalling gas cloud [81]. In practice, detecting photons circling around photon spheres several times at late times could be a challenging task due to the scarcity of these photons. Interestingly, it showed that precise measurements of photon rings, which are formed of photons circling around photon spheres more than once, may be feasible with a very long baseline interferometry [82–84]. Therefore, it is timely to study observational appearances of a freely-falling star in the wormhole background, which provides a new way to detect wormholes.

The rest of the paper is organized as follows. In Section II, we briefly review the asymmetric thin-shell wormhole and introduce our observational settings. Numerical results are presented in

Section III. Finally, we conclude with a brief discussion in Section IV. We set $G = c = 1$ throughout this paper.

II. SETUP

As introduced in [62, 65, 85], an asymmetric thin-shell wormhole has two distinct spacetimes, \mathcal{M}_1 and \mathcal{M}_2 , which are glued together by a thin shell at its throat. The metric of the wormhole is described as

$$ds_i^2 = -f_i(r_i)dt_i^2 + \frac{dr_i^2}{f_i(r_i)} + r_i^2 d\Omega^2, \quad (1)$$

where $i = 1$ and 2 indicate quantities in \mathcal{M}_1 and \mathcal{M}_2 , respectively. Focusing on the Schwarzschild spacetime, we have

$$f_i(r_i) = 1 - \frac{2M_i}{r_i} \text{ for } r_i \geq R, \quad (2)$$

where M_i are the mass parameters, and R is throat radius. Without loss of generality, we set $M_1 = 1$ and $M_2 = k$ in the rest of this paper. For more details of the asymmetric thin-shell wormhole, refer to [62]. In \mathcal{M}_1 and \mathcal{M}_2 , the local tetrads are

$$\mathbf{e}_{t_i} = f_i^{-\frac{1}{2}}(r_i) \frac{\partial}{\partial t_i}, \quad \mathbf{e}_{r_i} = f_i^{\frac{1}{2}}(r_i) \frac{\partial}{\partial r_i}, \quad \mathbf{e}_{\theta_i} = \frac{1}{r_i} \frac{\partial}{\partial \theta_i}, \quad \mathbf{e}_{\phi_i} = \frac{1}{r_i \sin(\theta)} \frac{\partial}{\partial \phi_i}. \quad (3)$$

At the throat, one has $\mathbf{e}_{t_1} = \mathbf{e}_{t_2}$, $\mathbf{e}_{r_1} = -\mathbf{e}_{r_2}$, $\mathbf{e}_{\theta_1} = \mathbf{e}_{\theta_2}$ and $\mathbf{e}_{\phi_1} = \mathbf{e}_{\phi_2}$, which yields the relations between the bases of the tangent space of \mathcal{M}_1 and \mathcal{M}_2 ,

$$\frac{\partial}{\partial t_1} = Z^{-1} \frac{\partial}{\partial t_2}, \quad \frac{\partial}{\partial r_1} = -Z \frac{\partial}{\partial r_2}, \quad \frac{\partial}{\partial \theta_1} = \frac{\partial}{\partial \theta_2}, \quad \frac{\partial}{\partial \phi_1} = \frac{\partial}{\partial \phi_2}, \quad (4)$$

where $Z \equiv \sqrt{f_2(R)/f_1(R)}$. Therefore, the components of a vector at the throat in \mathcal{M}_1 and \mathcal{M}_2 are related by

$$V^{t_1} = ZV^{t_2}, \quad V^{r_1} = -Z^{-1}V^{r_2}, \quad V^{\theta_1} = V^{\theta_2}, \quad V^{\phi_1} = V^{\phi_2}. \quad (5)$$

In this paper, we study a point-like star freely falling along the radial direction at $\theta_i = \pi/2$ and $\varphi_i = 0$, which emits photons isotropically in its rest frame. With spherical symmetry, we can confine ourselves to emissions on the equatorial plane. The geodesics on the equatorial plane are described by the Lagrangian

$$\mathcal{L} = -\frac{1}{2} \left[f_i(r_i) \dot{t}_i^2 + \frac{1}{f_i(r_i)} \dot{r}_i^2 + r_i^2 \dot{\varphi}_i^2 \right], \quad (6)$$

where dots stand for derivative with respect to an affine parameter τ . Since the Lagrangian \mathcal{L} does not depend on coordinates t_i and φ_i , the geodesics can be characterized by their conserved energy E_i and angular momentum l_i in \mathcal{M}_i ,

$$E_i = -p_{t_i} = f_i(r_i)\dot{t}_i, \quad l_i = p_{\varphi_i} = r_i^2\dot{\varphi}_i. \quad (7)$$

Note that, according to eqn. (5), one has $E_1 = E_2/Z$ and $l_1 = l_2$.

The Lagrangian of the freely-falling star obeys the constancy $\mathcal{L} = -1/2$ when the affine parameter τ is chosen as the proper time. Since the star falls radially, its angular momentum $l_i = 0$. Due to the traversability of the wormhole, we consider two scenarios with distinct trajectories of the star. In the scenario I, the star with energy $E_1 = 1/Z$ ($E_2 = 1$) has a nonzero initial velocity at spatial infinity of \mathcal{M}_1 . So, the star can pass through the throat and travel towards spatial infinity of \mathcal{M}_2 . With the relation (7), the four-velocities of the star in \mathcal{M}_1 and \mathcal{M}_2 are given by

$$\begin{aligned} v_e^{\mu_1}(r_1) &= \left(\frac{1}{1-2r_1^{-1}} \sqrt{\frac{R-2}{R-2k}}, -\sqrt{\frac{2k-2}{R-2k} + \frac{2}{r_1}}, 0, 0 \right), \\ v_e^{\mu_2}(r_2) &= \left(\frac{1}{1-2kr_2^{-1}}, \sqrt{\frac{2k}{r_2}}, 0, 0 \right). \end{aligned} \quad (8)$$

In the scenario II, the star with energy $E_1 = 1$ is initially at rest at spatial infinity of \mathcal{M}_1 . At first, the star falls freely in \mathcal{M}_1 , passes through the throat and reaches a turning point in \mathcal{M}_2 . Then, it moves towards the throat in \mathcal{M}_2 , returns to \mathcal{M}_1 and comes to rest at spatial infinity of \mathcal{M}_1 . Similarly, the four-velocities of the star in \mathcal{M}_1 and \mathcal{M}_2 are

$$\begin{aligned} v_e^{\mu_1}(r_1) &= \left(\frac{1}{1-2r_1^{-1}}, \mp \sqrt{\frac{2M}{r_1}}, 0, 0 \right), \\ v_e^{\mu_2}(r_2) &= \left(\frac{1}{1-2kr_2^{-1}} \sqrt{\frac{R-2k}{R-2}}, \pm \sqrt{\frac{-2k+2}{R-2} + \frac{2k}{r_2}}, 0, 0 \right), \end{aligned} \quad (9)$$

where plus and minus signs represent outward and inward moving, respectively.

Moreover, null geodesics on the equatorial plane are also governed by the Lagrangian (6) with $\mathcal{L} = 0$, which rewrites the radial component of the null geodesic equations as

$$\frac{\dot{r}_i^2}{L_i^2} = \frac{1}{b_i^2} - V_{i,\text{eff}}(r_i), \quad (10)$$

where $b_i \equiv l_i/E_i$ is the impact parameter, and $V_{i,\text{eff}}(r_i) = f_i(r_i)r_i^{-2}$ is the effective potential. Note that the impact parameters of a null geodesic in \mathcal{M}_1 and \mathcal{M}_2 , namely b_1 and b_2 , are related by $b_1 = Zb_2$. A photon sphere in \mathcal{M}_i is constituted of unstable circular null geodesics, whose radius r_i^{ph} is determined by

$$V_{i,\text{eff}}(r_i^{\text{ph}}) = \frac{1}{(b_i^{\text{ph}})^2}, \quad V'_{i,\text{eff}}(r_i^{\text{ph}}) = 0, \quad V''_{i,\text{eff}}(r_i^{\text{ph}}) < 0, \quad (11)$$

		Inward	Outward
Scenario I	\mathcal{M}_1	$\sqrt{\frac{R-2}{R-2k}} - \cos(\alpha)\sqrt{\frac{2k-2}{R-2k} + \frac{2}{r_e}}$	/
	\mathcal{M}_2	/	$\sqrt{\frac{R-2}{R-2k}} + \cos(\alpha)\sqrt{\frac{R-2}{R-2k}}\sqrt{\frac{2k}{r_e}}$
Scenario II	\mathcal{M}_1	$1 - \cos(\alpha)\sqrt{\frac{2}{r_e}}$	$1 + \cos(\alpha)\sqrt{\frac{2}{r_e}}$
	\mathcal{M}_2	$1 - \cos(\alpha)\sqrt{\frac{R-2}{R-2k}}\sqrt{\frac{-2k+2}{R-2} + \frac{2k}{r_e}}$	$1 + \cos(\alpha)\sqrt{\frac{R-2}{R-2k}}\sqrt{\frac{-2k+2}{R-2} + \frac{2k}{r_e}}$

TABLE I. The normalized frequency ω_o/ω_e as a function of the star position r_e and the emission angle α in the scenarios I and II. Inward and outward correspond to travelling towards and away from the throat, respectively.

where b_i^{ph} is the corresponding impact parameter. Photons with $b_i \approx b_i^{\text{ph}}$ are temporarily trapped at the photon sphere and can determine late-time observational appearances of the wormhole. If the throat radius satisfies $\max\{2, 2k\} < R < \min\{3, 3k\}$, the asymmetric thin-shell wormhole can be free of the event horizon and possess two photon spheres, which are located at $r_1^{\text{ph}} = 3$ and $r_2^{\text{ph}} = 3k$ in \mathcal{M}_1 and \mathcal{M}_2 , respectively. In this paper, we consider the asymmetric thin-shell wormhole with $k = 1.2$ and $R = 2.6$, whose observational appearance of an accretion disk has been discussed in [65].

We assume that the emitted photons are collected by distant observers distributed on a celestial sphere located at $r_1 = r_o$ in \mathcal{M}_1 . To trace light rays emitting from the star to a distant observer, one needs to supply initial conditions. For a photon of four-momentum p_{μ_i} , the momentum measured in the rest frame of the star with four-velocity $v_e^{\mu_i}$ at $r_i = r_e$ is

$$\begin{aligned}
p^{\hat{t}} &= -v_e^{t_i}(r_e)p_{t_i} - v_e^{r_i}(r_e)p_{r_i}, \\
p^{\hat{r}} &= -\sqrt{[v_e^{t_i}(r_e)]^2 - f_i^{-1}(r_e)}p_{t_i} \pm \sqrt{[v_e^{r_i}(r_e)]^2 + f_i(r_e)}p_{r_i}, \\
p^{\hat{\theta}} &= 0, \quad p^{\hat{\phi}} = \frac{p_{\varphi_i}}{r_e},
\end{aligned} \tag{12}$$

where plus and minus signs correspond to negative and positive $v_e^{r_i}$, respectively. The emission angle α is defined as

$$\cos \alpha = \frac{p^{\hat{r}}}{p^{\hat{t}}}, \tag{13}$$

which is the angle between the propagation direction of the photon and the radial direction in the rest frame of the star. In the rest frame, the photon is emitted with proper frequency $\omega_e = -(v_e^{\mu_i} p_{\mu_i})_e = p^{\hat{t}}$. For a distant static observer with four-velocity $v_o^{\mu_1} = (1, 0, 0, 0)$, the photon is observed with frequency $\omega_o = -(v_o^{\mu_1} p_{\mu_1})_o = p^{\hat{t}_1}$. With eqns. (5), (12) and (13), we express the

normalized frequency ω_o/ω_e as a function of the star position r_e and the emission angle α for two scenarios in Table. I. Furthermore, the luminosity of photons is given by $L_k = d\mathcal{E}_k/d\tau_k$, where \mathcal{E}_k is the total energy, τ_k is the proper time, and $k = e$ and o denote quantities corresponding to the emitter and the observer, respectively. Similar to the normalized frequency, one can define the normalized luminosity

$$\frac{L_o}{L_e} = \frac{d\mathcal{E}_o/d\tau_o}{d\mathcal{E}_e/d\tau_e} \approx \frac{\omega_o dn_o}{\omega_e dn_e} \left(\frac{dt_o}{d\tau_e} \right)^{-1}, \quad (14)$$

where n_o and n_e are the observed and emitted photon numbers, respectively, and we replaced $d\tau_o$ by dt_o since they are almost the same for distant observers.

III. NUMERICAL RESULTS

In this section, we numerically study observational appearances of a star freely falling radially in the asymmetric thin-shell wormhole in the scenarios I and II. During the free fall of the star, photons are emitted isotropically in the rest frame of the star. Specifically, we assume that the star starts emitting photons at $t_1 = t_2 = 0$ and $r_1 = 30.65$ in \mathcal{M}_1 , and emits 3200 photons, which are uniformly distributed in the emission angle α , every proper time interval $\delta\tau_e = 0.002$. It is worth emphasizing that observational appearances of the freely-falling star, especially late-time appearances, are rather insensitive to the initial position where the star starts emitting. Here, for better comparison with the Schwarzschild black hole case, we simply choose the initial position as $r_1 = 30.65$, which is in agreement with that of [76].

Here, observational appearances of the star are studied for two kinds of observers in \mathcal{M}_1 . The first kind is observers distributed on a celestial sphere at the radius $r_o = 100$, which refers to collecting photons in the whole sky at fixed radial coordinate $r_o = 100$ in \mathcal{M}_1 . The measurement by the observers on the celestial sphere would give the frequency distribution and the total luminosity of photons that reach the celestial sphere. The second kind is a specific observer, who is located at $\varphi_o = 0$ on the equator of the celestial sphere. Among all photons collected on the celestial sphere, we select photons with $\cos\varphi > 0.99$ to mimic photons detected by the specific observer. To calculate observed luminosities, the collected photons are grouped into packets of 50 (i.e., $dn_o = 50$) according to their arrival time.

As shown in FIG. 1, the asymmetric thin-shell wormhole with $k = 1.2$ and $R = 2.6$ has a double-peak effective potential, corresponding to one photon sphere in \mathcal{M}_1 and one in \mathcal{M}_2 . Specifically, the photon sphere in \mathcal{M}_1 is located at $r_1^{\text{ph}} = 3$ with the critical impact parameter $b_1^{\text{ph}} = 3\sqrt{3}$, and

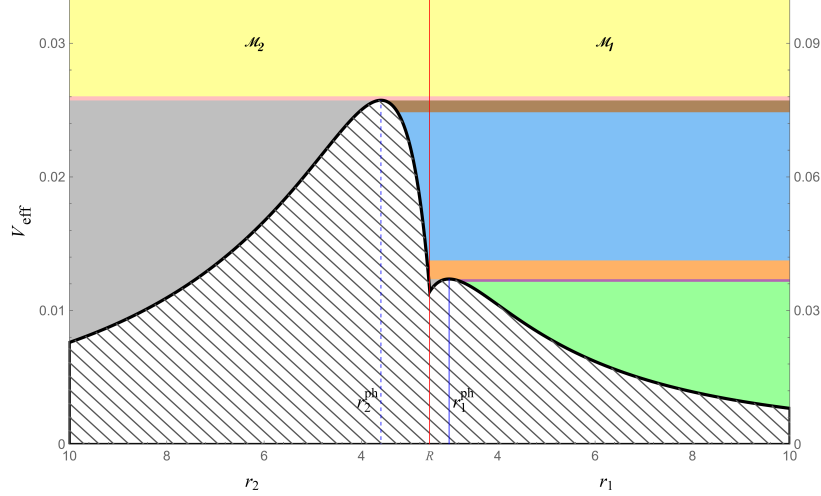


FIG. 1. The effective potential of null geodesics in the asymmetric thin-shell wormhole with $k = 1.2$ and $R = 2.6$. The potential has two peaks at $r_1^{\text{ph}} = 3$ (solid vertical blue line) and $r_2^{\text{ph}} = 3.6$ (dashed vertical blue line), corresponding to a photon sphere with $b_1^{\text{ph}} = 3\sqrt{3}$ in \mathcal{M}_1 and another one with $b_2^{\text{ph}} = 3.6\sqrt{3}$ in \mathcal{M}_2 , respectively. The vertical red line denotes the throat at $r_1 = r_2 = R$. Photons emitted in the pink, brown, orange and purple regions have impact parameters close to the impact parameters of the photon spheres, and hence can be temporarily trapped around the photon spheres. In particular, when photons are emitted towards the throat at $r_2 > r_2^{\text{ph}}$ in the pink region or at $r_1 > r_1^{\text{ph}}$ in the brown, orange and purple regions, they usually orbit the wormhole with $\Delta\varphi \geq 2\pi$.

that in \mathcal{M}_2 is located at $r_2^{\text{ph}} = 3.6$ with the critical impact parameter $b_2^{\text{ph}} = 3.6\sqrt{3}$. To discuss how photons with different impact parameters contribute to the observations of the star, we classify received photons into seven categories according to their impact parameter b_1 in \mathcal{M}_1 ,

- $b_1 < 3.579$. Yellow region in FIG. 1 and yellow dots in FIGs. 4, 5, 7 and 8.
- $3.579 \leq b_1 < Zb_2^{\text{ph}}$. Pink region in FIG. 1 and pink dots in FIGs. 4, 5, 7 and 8. In this category, photons emitted inward outside the photon sphere in \mathcal{M}_2 can circle around the photon sphere more than once before reaching a distant observer in \mathcal{M}_1 . For example, a light ray with $b_1 = 3.579$, which has $\Delta\varphi = 2\pi^1$, is displayed in the upper-left panel of FIG. 2.
- $Zb_2^{\text{ph}} < b_1 \leq 3.664$. Brown region in FIG. 1 and brown dots in FIGs. 4, 5, 7 and 8. In this category, photons emitted inward would circle around the photon sphere in \mathcal{M}_2 roughly with $\Delta\varphi \geq 2\pi$ before escaping to the celestial sphere in \mathcal{M}_1 . For example, a light ray with $b_1 = 3.664$, which has $\Delta\varphi = 2\pi$, is displayed in the upper-right panel of FIG. 2.

¹ Since $\varphi_1 = \varphi_2$ at the throat, the subscript of φ is omitted for simplicity.

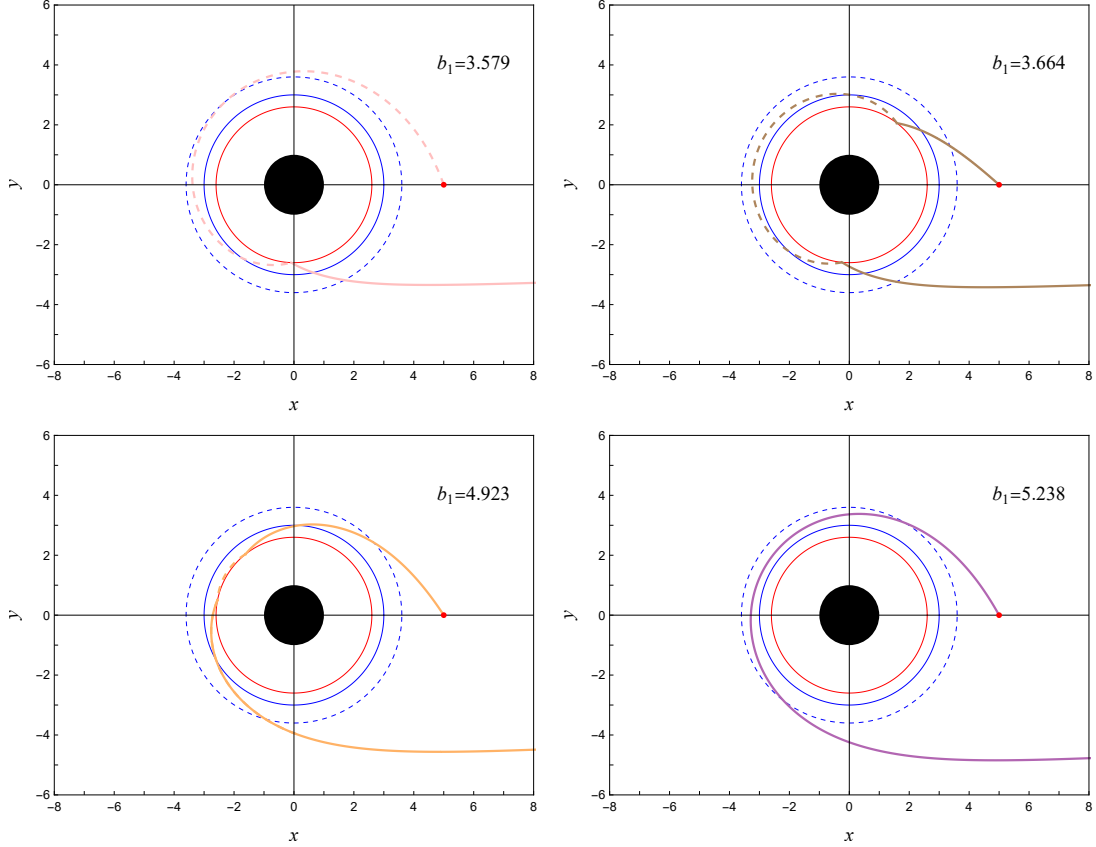


FIG. 2. Photon trajectories in the asymmetric thin-shell wormhole with $k = 1.2$ and $R = 2.6$. The red points and circles denote the star and the throat, respectively. The blue solid and dashed circles represent the photon spheres in \mathcal{M}_1 and \mathcal{M}_2 , respectively. The upper-left panel shows a photon emitted at $r_e = 5$ in \mathcal{M}_2 with $b_1 = 3.579$, and the light ray has $\Delta\varphi = 2\pi$. Other panels show photons emitted at $r_e = 5$ in \mathcal{M}_1 with $b_1 = 3.664, 4.923$ and 5.238 , and the light rays all have $\Delta\varphi = 2\pi$. The solid and dashed segments of the light rays correspond to the segments in \mathcal{M}_1 and \mathcal{M}_2 , respectively.

- $3.664 < b_1 \leq 4.923$. Blue region in FIG. 1 and blue dots in FIGs. 4, 5, 7 and 8.
- $4.923 < b_1 < b_1^{\text{ph}}$. Orange region in FIG. 1 and orange dots in FIGs. 4, 5, 7 and 8. In this category, if photons are emitted inward outside the photon sphere in \mathcal{M}_1 , they would linger for some time around the photon sphere by orbiting it approximately with $\Delta\varphi \geq 2\pi$. For example, a light ray with $b_1 = 4.923$, which has $\Delta\varphi = 2\pi$, is displayed in the lower-left panel of FIG. 2.
- $b_1^{\text{ph}} < b_1 \leq 5.238$. Purple region in FIG. 1 and purple dots in FIGs. 4, 5, 7 and 8. In this category, photons emitted inward outside the photon sphere in \mathcal{M}_1 usually circle around the photon sphere more than once. For example, a light ray with $b_1 = 5.238$, which has

$\Delta\varphi = 2\pi$, is displayed in the lower-right panel of FIG. 2.

- $b_1 > 5.238$. Green region in FIG. 1 and green dots in FIGs. 4, 5, 7 and 8.

In short, we use the orbit number of light rays emitted at $r_1 = 5$ in \mathcal{M}_1 or $r_2 = 5$ in \mathcal{M}_2 to determine the threshold impact parameters separating the seven categories. To sum up, light rays emitted inward at $r_2 = 5$ in the yellow/pink category would circle around the wormhole less/more than once before being received; light rays emitted inward at $r_1 = 5$ would circle around the wormhole less than once before being received in the blue and green categories, or more than once in the brown, orange and purple categories. Note that the orbit number of light rays with a given impact parameter depends slightly on the emitting position. So, light rays connecting the star and the observers circle around the wormhole approximately more than once in the pink, brown, orange and purple categories, and less than once in the yellow, blue and green categories. In other words, photons in the pink, brown, orange and purple categories can be temporarily trapped near the photon spheres.

A. Scenario I

In the scenario I, the star with energy $E_1 = 1/Z = \sqrt{3}$ would travel through the throat and move towards spatial infinity of \mathcal{M}_2 . For near-critical photons emitted with the impact parameter very close to those of the photon spheres in \mathcal{M}_1 (i.e., $b_1 \simeq b_1^{\text{ph}}$) and \mathcal{M}_2 (i.e., $b_2 \simeq b_2^{\text{ph}}$), their normalized frequencies ω_o/ω_e measured by observers on the celestial sphere are plotted against the emitted position r_e in FIG. 3. The colors of the lines in FIG. 3 match those of the corresponding emitted regions in FIG. 1. Moreover, photons with $b_1 \simeq b_1^{\text{ph}}$ and $b_2 \simeq b_2^{\text{ph}}$ are denoted by solid and dashed lines, respectively. It is worth emphasizing that the observed frequency of a photon is determined by the gravitational redshift and the Doppler effect, which are controlled by the position and the velocity of the photon when it is emitted, respectively.

For photons of $b_2 \simeq b_2^{\text{ph}}$, the normalized frequency can noticeably exceed 1 at a large r_e in \mathcal{M}_1 since the Doppler effect plays a more important role than the gravitational redshift. As the star falls towards the throat, the normalized frequency decreases due to stronger gravitational redshift, and blueshift becomes redshift at $r_e = 4.063$ in \mathcal{M}_1 , where the normalized frequency is 1. When emitted at the throat, the normalized frequency reaches the minimum. After the star enters \mathcal{M}_2 , the normalized frequency increases as r_e grows, and observed photons become bluishifted when $r_e > 12.281$. For photons of $b_1 \simeq b_1^{\text{ph}}$, the behavior of the normalized frequency is quite similar to

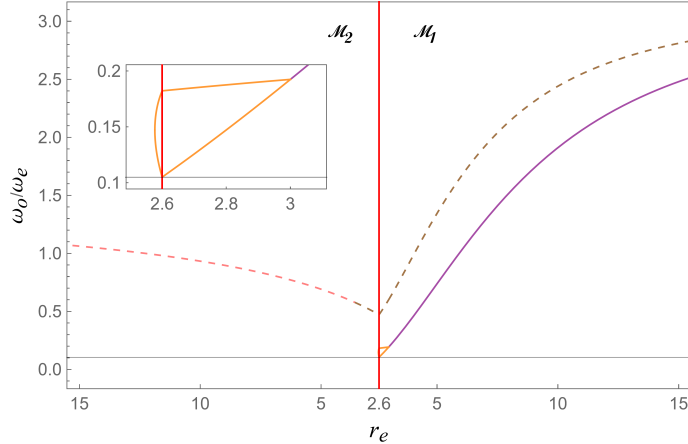


FIG. 3. The normalized frequency ω_o/ω_e as a function of the emitted position r_e for photons in the scenario I, whose impact parameter is very close to these of the photon spheres in \mathcal{M}_1 (solid lines) and \mathcal{M}_2 (dashed lines). The observers are distributed on the celestial sphere at $r_o = 100$ in \mathcal{M}_1 . For a large r_e in \mathcal{M}_1 , inward-emitted and near-critical photons can be blueshifted since the Doppler effect dominates over the gravitational redshift. Due to the relation (5) at the throat, near-critical photons can also be blueshifted when r_e is large in \mathcal{M}_2 . Photons emitted inward and outward between the two photon spheres can both reach a distant observer after orbiting the photon sphere in \mathcal{M}_1 , which gives two branches of the orange line in the inset. Moreover, the normalized frequency reaches the minimum at the throat, which is located at $r_e = 2.6$.

those of $b_2 \simeq b_2^{\text{ph}}$ when they are emitted outside the photon sphere in \mathcal{M}_1 . When the star emits photons between the two photon spheres, inward-emitted and outward-emitted photons can both be captured by a distant observer after they circle around the photon sphere in \mathcal{M}_1 , thus leading to two branches as shown in the inset. The upper and lower branches correspond to photons emitted away from and towards the observer, respectively.

In the left panel of FIG. 4, we display the normalized frequency distribution of photons, which are emitted from the freely-falling star in the scenario I and collected by observers distributed on the celestial sphere at $r_o = 100$ in \mathcal{M}_1 . At early times, received photons are dominated by those emitted in the green region of FIG. 1, among which inward-emitted photons contribute to the high-frequency observation. When $t_o > 160$, photons emitted towards the photon sphere in \mathcal{M}_2 in the blue and brown regions start reaching the observers after orbiting around the photon sphere. Subsequently, the observers receive photons emitted towards the photon sphere in \mathcal{M}_1 in the purple and orange regions. Since time moves faster in \mathcal{M}_2 roughly by a factor of $1/Z = \sqrt{3}$ relative to in \mathcal{M}_1 , photons circling around the photon sphere in \mathcal{M}_2 arrive earlier. Moreover, the maximum frequency of photons emitted in the blue and brown regions is higher than that of

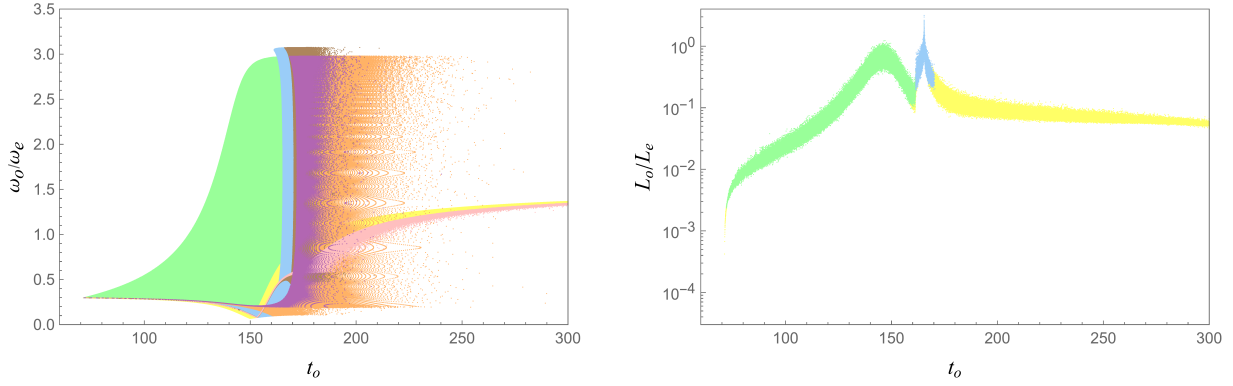


FIG. 4. The normalized frequency distribution and the total luminosity of the freely-falling star in the scenario I, measured by observers on a celestial sphere at $r_o = 100$ in \mathcal{M}_1 . **Left:** The observers receive photons with a wide range of frequencies. At the early stage, photons emitted in the green region of FIG. 1 give rise to the frequency observation. Afterwards, photons emitted in the brown, blue, orange and purple regions are observed. In particular, photons with a near-critical impact parameter produce high frequency observations. The late-time frequency observation is determined by photons in the yellow and pink regions, which are emitted at a large r_e in \mathcal{M}_2 . **Right:** The luminosity is calculated by grouping received photons into packets of 50. An increase of the observed luminosity is caused by photons emitted inward in the blue region, leading to a peak at $t_o \simeq 168$. At late times, the total luminosity gradually decays with time and is mainly controlled by photons, which are emitted at a large r_e in \mathcal{M}_2 and travel through the throat to reach the observers.

photons emitted in the green, purple and orange regions. This is expected from FIG. 3, which shows that near-critical photons with $b_2 \simeq b_2^{\text{ph}}$ have higher normalized frequency than these with $b_1 \simeq b_1^{\text{ph}}$. Afterwards, the frequency observations are dominated by photons emitted in the orange region, which are trapped at the photon sphere in \mathcal{M}_1 for a longer time. At late times, the observers mostly receive photons in the yellow and pink regions, which are emitted towards the throat in \mathcal{M}_2 with a small impact parameter.

The normalized total luminosity of the freely-falling star is displayed in the right panel of FIG. 4, where a dot corresponds to a packet of 50 photons, and the color of the dot is that having most photons in the packet. The luminosity gradually increases until reaching a peak around $t_o \simeq 145$, and is dominated by photons emitted in the green region roughly before $t_o = 150$, which is in agreement with the frequency observation. After $t_o \simeq 160$, photons emitted in the blue region give rise to a noticeable increase of the total luminosity. As the star moves towards spatial infinity of \mathcal{M}_2 , emitted photons can still propagate to the observers in \mathcal{M}_1 through the throat, and a slight decrease of the total luminosity is displayed at late times. Interestingly, this late-time observation

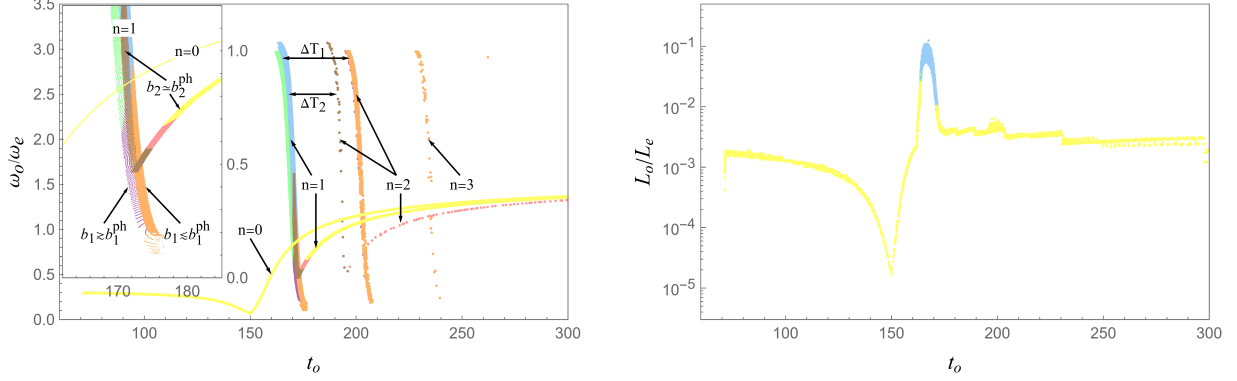


FIG. 5. The normalized frequency and the luminosity of the freely-falling star in the scenario I, measured by a distant observer at $r_o = 100$, $\theta_o = \pi/2$ and $\phi_o = 0$ in \mathcal{M}_1 . The colored dots denote photons emitted in the regions with the same color in FIG. 1. **Left:** Received photons form several frequency lines indexed by the orbiting number n . The inset displays three frequency lines caused by $n = 1$ photons with $b_1 \gtrsim b_1^{\text{ph}}$, $b_1 \lesssim b_1^{\text{ph}}$ and $b_2 \simeq b_2^{\text{ph}}$. The time delay between the adjacent $n \geq 1$ lines formed by photons orbiting around the photon sphere in \mathcal{M}_1 and \mathcal{M}_2 is roughly the period of circular null geodesics at the photon sphere, i.e., $\Delta T_1 \simeq 2\pi b_1^{\text{ph}} \simeq 33$ and $\Delta T_2 \simeq 2\pi Z b_2^{\text{ph}} \simeq 23$, respectively. **Right:** At early times, the luminosity is dominated by photons with a small impact parameter, and decreases first and then increases after the star goes through the throat. Subsequently, blueshifted $n = 1$ photons start to reach the observer and become the most dominant contribution, which produces a luminous flash at $t_o \simeq 170$. Later, the luminosity is mainly contributed by the $n = 0$ photons emitted in the yellow region of \mathcal{M}_2 and almost declines gradually at late times. In addition, a faint flash, which results from the $n = 2$ photons emitted in the orange region, is observed at $t_o \simeq 200$.

is strikingly different from the black hole case, where the total luminosity has been found to decay exponentially at late times [76, 77].

For a specific observer located at $\varphi_o = 0$ and $\theta_o = \pi/2$ on the celestial sphere at $r_o = 100$ in \mathcal{M}_1 , the angular coordinate change $\Delta\varphi$ of light rays connecting the star with the observer is

$$\Delta\varphi = 2n\pi, \quad (15)$$

where $n = 0, 1, 2, \dots$ is the number of orbits that the light rays complete around the wormhole. To simulate observational appearances of the star seen by the observer, we select photons with $\cos\varphi > 0.99$ from all photons received on the celestial sphere. The frequency observation is presented in the left panel of FIG. 5, which shows a discrete spectrum separated by the received time. The yellow line is formed by photons with $n = 0$, which radially propagate to the observer. At early times, the observed frequency of the $n = 0$ photons decreases with the received time as the star falls towards the throat. After the star passes through the throat, the observed frequency

of the $n = 0$ photons increases since the gravitational redshift becomes weaker as the star moves further away from the throat, which results in the dip at $t_o \simeq 150$. Owing to the existence of two photon spheres, the $n = 1$ photons with impact parameters $b_1 \gtrsim b_1^{\text{ph}}$, $b_1 \lesssim b_1^{\text{ph}}$ and $b_2 \simeq b_2^{\text{ph}}$ can form three frequency lines, which are highlighted in the inset of FIG. 5. As the star falls towards the throat, the three frequency lines decrease rapidly due to strong gravitational redshift near the throat. After the star passes through the throat, the frequency line with $b_2 \simeq b_2^{\text{ph}}$ gradually increases. For $n = 2$, the frequency lines with $b_1 \gtrsim b_1^{\text{ph}}$ and $b_1 \lesssim b_1^{\text{ph}}$ move closer and are hardly distinguishable from each other. On the other hand, the frequency line with $b_2 \simeq b_2^{\text{ph}}$ becomes more separate from them since photons spend more time orbiting around the photon sphere in \mathcal{M}_1 . Indeed, it takes $\Delta T_1 \simeq 2\pi b_1^{\text{ph}} \simeq 33$ to orbit around the photon sphere in \mathcal{M}_1 one time, and $\Delta T_2 \simeq 2\pi Z b_2^{\text{ph}} \simeq 23$ to orbit around that in \mathcal{M}_2 ². Therefore, for $b_1 \gtrsim b_1^{\text{ph}}$ and $b_1 \lesssim b_1^{\text{ph}}$ ($b_2 \simeq b_2^{\text{ph}}$), the time delay between the $n = 1$ and 2 frequency lines roughly equals to ΔT_1 (ΔT_2). For $n = 3$, because of the finite number of photons in our numerical simulation, only the frequency line with $b_2 \gtrsim b_2^{\text{ph}}$ can be found and is shown by orange dots around $t_o \simeq 230$.

The left panel of FIG. 5 shows the observed normalized luminosity as a function of the time, which exhibits a decline before the star reaches the throat. After the star moves through the throat, the luminosity starts to increase since the frequency of received photons grows, which causes a dip at $t_o \simeq 150$. Around $t_o \simeq 160$, blueshifted photons with $n = 1$ start to play a dominant role, leading to a luminous flash around $t_o \simeq 170$. Afterwards, the luminosity is mainly dominated by photons emitted in the yellow region of \mathcal{M}_2 , and slowly decreases except a faint flash at $t_o \simeq 200$ caused by the arrival of $n = 2$ photons. The flashes of photons with $n \geq 3$ are much fainter and barely visible in the background of the dominant photons emitted in the yellow region. In contrast, for a black hole with two photon spheres, a series of flashes with decreasing luminosity are observed at late times due to photons orbiting around the hairy black hole different times [77].

B. Scenario II

In the scenario II, the star starts falling from spatial infinity of \mathcal{M}_1 and returns to the infinity after going through the throat twice. Similarly, the normalized frequency ω_o/ω_e for near-critical photons is plotted in FIG. 6. Specifically, we focus on photons with $b_1 \simeq b_1^{\text{ph}}$ emitted in the purple and orange regions and those with $b_2 \simeq b_2^{\text{ph}}$ emitted in the brown region, which are denoted by solid and dashed lines, respectively. For photons with $b_1 \simeq b_1^{\text{ph}}$ emitted outside the photon sphere in

² Eqn. (7) leads to $dt/d\phi|_{r^{\text{ph}}} = b^{-1}V_{\text{eff}}^{-1}(r^{\text{ph}}) = b^{\text{ph}}$, which gives $\Delta T \simeq 2\pi b^{\text{ph}}$.

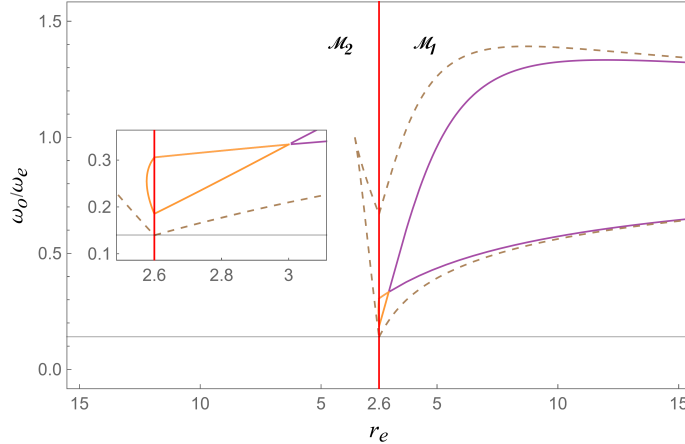


FIG. 6. The normalized frequency ω_o/ω_e as a function of the emitted position r_e for photons in the scenario II, whose impact parameter b_1 is very close to b_1^{ph} (solid lines) or b_2 is very close to b_2^{ph} (dashed lines). The observers are distributed on the celestial sphere at $r_o = 100$ in \mathcal{M}_1 . The normalized frequency of near-critical photons emitted in the purple and brown regions has two branches. Specifically, the high-frequency (low-frequency) branch corresponds to photons emitted from the star falling away (towards) from the observer. Similar to the scenario I, the high-frequency branch can be blueshifted for a large r_e in \mathcal{M}_1 . The normalized frequency reaches the global minimum $\omega_o/\omega_e \simeq 0.139$ at the throat for the low-frequency branch.

\mathcal{M}_1 (i.e., the purple region) and those with $b_2 \simeq b_2^{\text{ph}}$, the normalized frequency has high-frequency and low-frequency branches, corresponding to the star falling away from and towards the observer, respectively. If photons are emitted inside the photon sphere in \mathcal{M}_1 with $b_1 \simeq b_1^{\text{ph}}$, the high-frequency (low-frequency) branch denotes ingoing and outgoing (outgoing and ingoing) emissions from the star falling away from and towards the observer, respectively. For the high-frequency branches, strong gravitational lensing around the photon spheres can cause blueshifts of near-critical photons emitted inward at a large r_e in \mathcal{M}_1 . In particular, the normalized frequency with $b_1 \simeq b_1^{\text{ph}}$ ($b_2 \simeq b_2^{\text{ph}}$) reaches the maximum $\omega_o/\omega_e = 4/3$ ($\omega_o/\omega_e = 1.392$) at $r_e = 12$ ($r_e = 8.679$), becomes one at $r_e = 5.196$ ($r_e = 3.6$), and reaches the minimum $\omega_o/\omega_e = 0.306$ ($\omega_o/\omega_e = 0.139$) at the throat. In \mathcal{M}_2 , the normalized frequency with $b_2 \simeq b_2^{\text{ph}}$ reaches the maximum $\omega_o/\omega_e = 1$ at $r_e = 3.6$, where the star returns.

The normalized frequency distribution of photons received by observers distributed on the celestial sphere is presented in the left panel of FIG. 7. When $t_o \lesssim 200$, a wide range of frequencies is observed for photons emitted in the green region. After near-critical photons emitted in the purple, orange, blue and brown regions start arriving at the observers around $t_o \simeq 150$, they come to dominate the high-frequency part of the frequency distribution. This early-stage frequency distribution bears a resemblance to the Schwarzschild black hole case, in which a star falls from

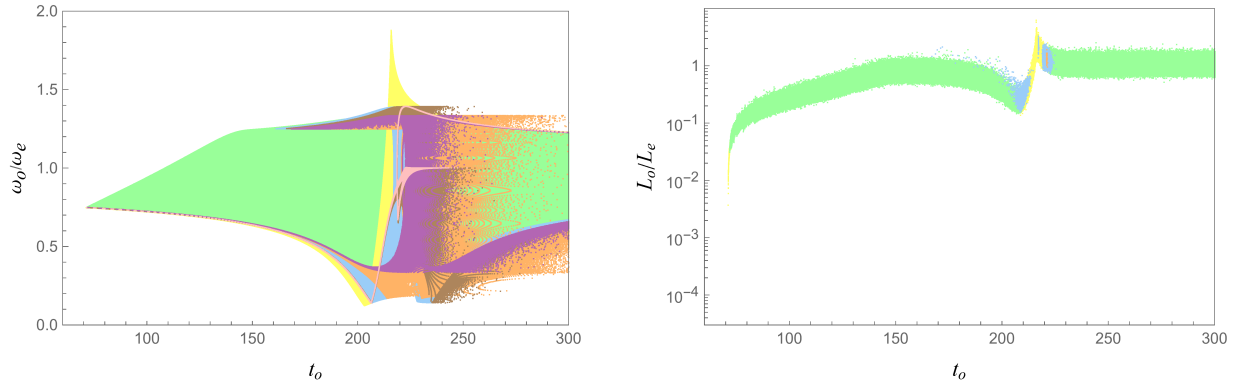


FIG. 7. The normalized frequency distribution (**Left**) and the total luminosity (**Right**) of the freely-falling star in the scenario II, measured by observers on the celestial sphere at $r_o = 100$ in \mathcal{M}_1 . Similar to the scenario I, photons emitted in the green region of FIG. 1 dominate the frequency and luminosity observations in the early stage. After the star enters \mathcal{M}_2 , photons emitted in the yellow region, which propagates to the observers nearly in the radial direction, produce frequency and luminosity peaks around $t_o \simeq 220$. Later, near-critical photons with a wide range of frequencies are observed. At late times, the emitted position r_e is in \mathcal{M}_1 and large, and therefore the observers would collect most of emitted photons, which leads to a nearly constant total luminosity.

spatial infinity at rest [76]. Similar to the scenario I, the maximum frequency of photons emitted inward in the blue and brown regions is greater than that of photons emitted inward in the green, purple and orange regions. After the star enters \mathcal{M}_2 , the observed frequency of photons emitted in the yellow region starts to increase and reaches a maximum around $t_o \simeq 220$, which is associated with the star returning to the throat. Subsequently, photons emitted in the brown and purple regions are observed to have a wide range of frequencies after they circle around the photon sphere in \mathcal{M}_1 and reach the observers. At late times, the star comes back to \mathcal{M}_1 and moves towards the observer, and thus the low-frequency distribution is dominated by photons emitted towards the throat with $b_1 \simeq b_1^{\text{ph}}$ and $b_2 \simeq b_2^{\text{ph}}$. On the other hand, photons emitted towards the observers with a small impact parameter produce the high-frequency observation.

The normalized total luminosity of the freely-falling star in the scenario II is displayed in the right panel of FIG. 7. Before $t_o \simeq 200$, the total luminosity behaves similarly to the Schwarzschild black hole case studied in [76], which is in consistency with the frequency observation. Afterwards, the received blueshifted photons with a small impact parameter dominate the total luminosity, resulting in a peak at $t_o \simeq 220$. At late times, the total luminosity is maintained around one since most emitted photons can be collected by the observers.

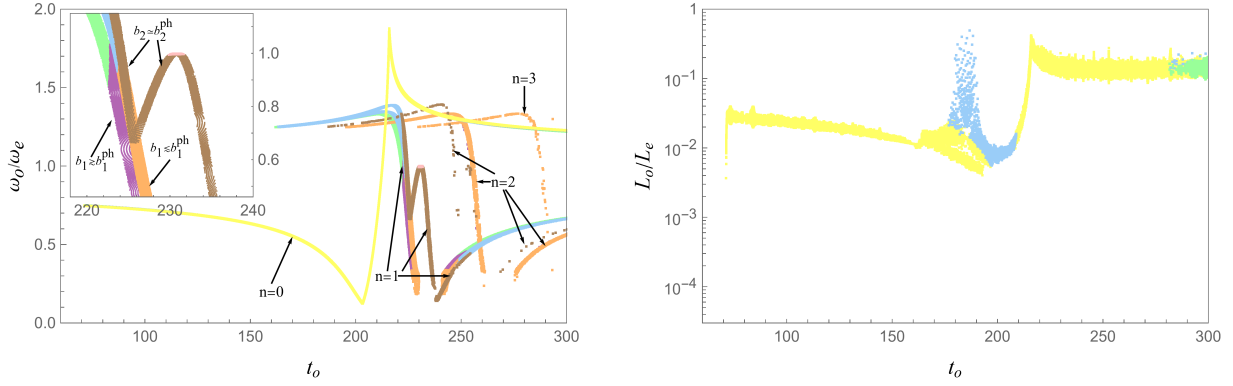


FIG. 8. The normalized frequency and the luminosity of the freely-falling star in the scenario II, measured by a distant observer at $r_o = 100$, $\theta = \pi/2$ and $\phi = 0$ in \mathcal{M}_1 . **Left:** The yellow line denotes radially emitted photons with $n = 0$ and has a dip (peak) near $t_o \simeq 200$ ($t_o \simeq 220$), corresponding to emission from the star at the throat. The $n = 1$ frequency lines with $b_1 \gtrsim b_1^{\text{ph}}$, $b_1 \lesssim b_1^{\text{ph}}$ and $b_2 \simeq b_2^{\text{ph}}$ steadily increase to a peak followed by a sharp decrease when $t_o \lesssim 230$, and gradually increase when $t_o \gtrsim 240$. For $230 \lesssim t_o \lesssim 240$, the $n = 1$ frequency line with $b_2 \simeq b_2^{\text{ph}}$ rises to another high point. **Right:** Similar to the scenario I, the luminosity is dominated by $n = 0$ photons and gradually decreases before $t_o \simeq 160$. Later, blueshifted $n = 1$ photons start to reach the observer and then become the most dominant contribution, which results in a luminosity peak around $t_o \simeq 180$. Afterwards, due to the increasing frequency of $n = 0$ photons emitted in \mathcal{M}_2 , the luminosity rises and reaches a peak around $t_o \simeq 220$. At late times, received $n = 0$ photons emitted in \mathcal{M}_1 enable the luminosity to stay roughly constant.

In the left panel of FIG. 8, we exhibit the normalized frequency of photons received by an observer located at $\varphi = 0$ and $\theta = \pi/2$ on the celestial sphere in \mathcal{M}_1 for the scenario II. The observed frequency of radially emitted photons with $n = 0$ is represented by the yellow line, which displays three periods. In the first and last periods, the photons are emitted when the star moves towards and away from the throat in \mathcal{M}_1 , respectively, and the $n = 0$ frequency line both decreases with the received time; in the intermediate period, the star emits the photons in \mathcal{M}_2 , and the $n = 0$ frequency line increases. There appears a peak and a dip of the $n = 0$ frequency line, which correspond to the star going through the throat the first time and the second time, respectively. Similar to the scenario I, the $n = 1$ frequency lines consist of three lines with $b_1 \gtrsim b_1^{\text{ph}}$, $b_1 \lesssim b_1^{\text{ph}}$ and $b_2 \simeq b_2^{\text{ph}}$, respectively. The $n = 1$ frequency line with $b_2 \simeq b_2^{\text{ph}}$ increases slowly until the maximum and then decreases rapidly in the first period, rises to a peak followed by a steep decline in the intermediate period, and gradually increases in the last period. For the $n = 1$ frequency lines with $b_1 \gtrsim b_1^{\text{ph}}$ and $b_1 \lesssim b_1^{\text{ph}}$, there is a sharp drop after reaching a peak when the star moves away from the observer, and a steady increase when the star moves towards the observer. For $n = 2$, only

two frequency lines are visible, namely the $b_1 \lesssim b_1^{\text{ph}}$ (orange dots) and $b_2 \simeq b_2^{\text{ph}}$ (brown dots) lines. Note that the $n = 2$ frequency lines are quite similar to the $n = 1$ counterparts. In addition, only the frequency line with $b_1 \lesssim b_1^{\text{ph}}$ is visible for $n = 3$.

The normalized luminosity of the star in the scenario II measured by the observer is displayed in the right panel of FIG. 8. Similar to the scenario I, the luminosity decreases slowly before $t_o \simeq 170$, which is dominated by radially emitted photons in the yellow region. Afterwards, photons emitted in the blue region come to control the luminosity observation and lead to a flash around $t_o \simeq 180$. Subsequently, photons emitted in the yellow region determine the luminosity observation again and produce a peak around $t_o \simeq 220$. At late times, the star travels towards the observer at a large r_e in \mathcal{M}_1 , and hence radially emitted photons would make a dominant contribution to the total luminosity. In particular, the late-time luminosity remains fairly constant, which is greatly different from the black hole case.

IV. CONCLUSIONS

In this paper, we investigated observational appearances of a point-like freely-falling star, which emits photons isotropically in its rest frame, in an asymmetric thin-shell wormhole connecting two spacetimes, \mathcal{M}_1 and \mathcal{M}_2 . Specifically, two scenarios with different initial velocities of the star were considered. In the scenario I, the star starts with a nonzero velocity at spatial infinity of \mathcal{M}_1 and moves towards spatial infinity of \mathcal{M}_2 . In the scenario II, the star falls at rest from spatial infinity of \mathcal{M}_1 , reaches a turning point in \mathcal{M}_2 and returns to \mathcal{M}_1 . For the two scenarios, the frequency distribution and luminosity of the star measured by all observers and a specific observer on a celestial sphere were obtained by numerically tracing emitted light rays. Interestingly, it was found that the absence of the event horizon and the presence of two photon spheres play a pivotal role in frequency and luminosity observations.

In [76] and [77], observational appearances of a star freely falling in black holes with one or two photon spheres were investigated. To compare the wormhole case with the black hole one, we briefly summarize the main findings of [76, 77] and this paper as follows.

- Black holes with a single photon sphere: The total luminosity of the star fades out with an exponentially decaying tail, which is determined by quasinormal modes at the photon sphere. At late times, the specific observer sees a series of flashes indexed by the orbit number, whose luminosity decreases exponentially with the orbit number. Moreover, the frequency content

of received photons contains a discrete spectrum of frequency lines indexed by the orbit number, which decay sharply at late times.

- Black holes with double photon spheres: At late times, the total luminosity first rises to a peak and then decreases with an exponentially decaying tail. The sub-long-lived quasinormal modes at the outer photon sphere are responsible for the slowly decaying exponential tail, and the leakage of photons trapped between the inner and outer photon spheres results in the luminosity peak. The specific observer sees two series of flashes, which are mainly determined by photons orbiting outside the outer and inner photon spheres, respectively. Moreover, the specific observer detects a discrete spectrum of frequency lines indexed by the orbit number and the photon sphere that received photons orbit around, which fall steeply at late times.
- Wormhole: At late times, the total luminosity first rises to a peak and then gradually decays with time (scenario I) or remains roughly constant (scenario II). The luminosity peak is caused by photons travelling between the two photon spheres (scenario I) or those emitted in \mathcal{M}_2 nearly along the radial direction (scenario II). Due to the absence of the event horizon, a considerable number of photons can still reach observers at late times, and hence an exponentially decaying tail would not appear. Similarly, the late-time luminosity measured by the specific observer can be sizable, and therefore he only sees a bright flash and a faint one (scenario I) or two bright flashes (scenario II) due to strong background luminance. Moreover, the specific observer detects frequency lines indexed by the orbit number and the photon sphere that received photons orbit around. The frequency lines produced by photons orbiting around the photon sphere in \mathcal{M}_1 decline sharply (scenario I) or grow steadily (scenario II) at late times; those produced by photons orbiting around the photon sphere in \mathcal{M}_2 gradually increase at late times.

In short, we showed that the absence of the event horizon in wormholes gives rise to significantly different optical appearances of a luminous star accreted onto wormholes at late times. Therefore, these findings can provide us a novel tool to distinguish wormholes from black holes in future observations.

ACKNOWLEDGMENTS

We are grateful to Guangzhou Guo and Qingyu Gan for useful discussions and valuable comments. This work is supported in part by NSFC (Grant No. 11875196, 11947225, 12105191, 12275183 and 12275184). Houwen Wu is supported by the International Visiting Program for Excellent Young Scholars of Sichuan University.

-
- [1] Kazunori Akiyama et al. First M87 Event Horizon Telescope Results. I. The Shadow of the Supermassive Black Hole. *Astrophys. J. Lett.*, 875:L1, 2019. [arXiv:1906.11238](https://arxiv.org/abs/1906.11238), [doi:10.3847/2041-8213/ab0ec7](https://doi.org/10.3847/2041-8213/ab0ec7). I
 - [2] Kazunori Akiyama et al. First M87 Event Horizon Telescope Results. II. Array and Instrumentation. *Astrophys. J. Lett.*, 875(1):L2, 2019. [arXiv:1906.11239](https://arxiv.org/abs/1906.11239), [doi:10.3847/2041-8213/ab0c96](https://doi.org/10.3847/2041-8213/ab0c96).
 - [3] Kazunori Akiyama et al. First M87 Event Horizon Telescope Results. III. Data Processing and Calibration. *Astrophys. J. Lett.*, 875(1):L3, 2019. [arXiv:1906.11240](https://arxiv.org/abs/1906.11240), [doi:10.3847/2041-8213/ab0c57](https://doi.org/10.3847/2041-8213/ab0c57).
 - [4] Kazunori Akiyama et al. First M87 Event Horizon Telescope Results. IV. Imaging the Central Supermassive Black Hole. *Astrophys. J. Lett.*, 875(1):L4, 2019. [arXiv:1906.11241](https://arxiv.org/abs/1906.11241), [doi:10.3847/2041-8213/ab0e85](https://doi.org/10.3847/2041-8213/ab0e85).
 - [5] Kazunori Akiyama et al. First M87 Event Horizon Telescope Results. V. Physical Origin of the Asymmetric Ring. *Astrophys. J. Lett.*, 875(1):L5, 2019. [arXiv:1906.11242](https://arxiv.org/abs/1906.11242), [doi:10.3847/2041-8213/ab0f43](https://doi.org/10.3847/2041-8213/ab0f43).
 - [6] Kazunori Akiyama et al. First M87 Event Horizon Telescope Results. VI. The Shadow and Mass of the Central Black Hole. *Astrophys. J. Lett.*, 875(1):L6, 2019. [arXiv:1906.11243](https://arxiv.org/abs/1906.11243), [doi:10.3847/2041-8213/ab1141](https://doi.org/10.3847/2041-8213/ab1141).
 - [7] Kazunori Akiyama et al. First M87 Event Horizon Telescope Results. VII. Polarization of the Ring. *Astrophys. J. Lett.*, 910(1):L12, 2021. [arXiv:2105.01169](https://arxiv.org/abs/2105.01169), [doi:10.3847/2041-8213/abe71d](https://doi.org/10.3847/2041-8213/abe71d).
 - [8] Kazunori Akiyama et al. First M87 Event Horizon Telescope Results. VIII. Magnetic Field Structure near The Event Horizon. *Astrophys. J. Lett.*, 910(1):L13, 2021. [arXiv:2105.01173](https://arxiv.org/abs/2105.01173), [doi:10.3847/2041-8213/abe4de](https://doi.org/10.3847/2041-8213/abe4de). I
 - [9] Kazunori Akiyama et al. First Sagittarius A* Event Horizon Telescope Results. I. The Shadow of the Supermassive Black Hole in the Center of the Milky Way. *Astrophys. J. Lett.*, 930(2):L12, 2022. [doi:10.3847/2041-8213/ac6674](https://doi.org/10.3847/2041-8213/ac6674). I
 - [10] Kazunori Akiyama et al. First Sagittarius A* Event Horizon Telescope Results. II. EHT and Multiwavelength Observations, Data Processing, and Calibration. *Astrophys. J. Lett.*, 930(2):L13, 2022. [doi:10.3847/2041-8213/ac6675](https://doi.org/10.3847/2041-8213/ac6675).
 - [11] Kazunori Akiyama et al. First Sagittarius A* Event Horizon Telescope Results. III. Imaging of the

- Galactic Center Supermassive Black Hole. *Astrophys. J. Lett.*, 930(2):L14, 2022. [doi:10.3847/2041-8213/ac6429](https://doi.org/10.3847/2041-8213/ac6429).
- [12] Kazunori Akiyama et al. First Sagittarius A* Event Horizon Telescope Results. IV. Variability, Morphology, and Black Hole Mass. *Astrophys. J. Lett.*, 930(2):L15, 2022. [doi:10.3847/2041-8213/ac6736](https://doi.org/10.3847/2041-8213/ac6736).
- [13] Kazunori Akiyama et al. First Sagittarius A* Event Horizon Telescope Results. V. Testing Astrophysical Models of the Galactic Center Black Hole. *Astrophys. J. Lett.*, 930(2):L16, 2022. [doi:10.3847/2041-8213/ac6672](https://doi.org/10.3847/2041-8213/ac6672).
- [14] Kazunori Akiyama et al. First Sagittarius A* Event Horizon Telescope Results. VI. Testing the Black Hole Metric. *Astrophys. J. Lett.*, 930(2):L17, 2022. [doi:10.3847/2041-8213/ac6756](https://doi.org/10.3847/2041-8213/ac6756). I
- [15] Farruh Atamurotov, Sushant G. Ghosh, and Bobomurat Ahmedov. Horizon structure of rotating Einstein–Born–Infeld black holes and shadow. *Eur. Phys. J. C*, 76(5):273, 2016. [arXiv:1506.03690](https://arxiv.org/abs/1506.03690), [doi:10.1140/epjc/s10052-016-4122-9](https://doi.org/10.1140/epjc/s10052-016-4122-9). I
- [16] Zdenek Stuchlík and Jan Schee. Shadow of the regular Bardeen black holes and comparison of the motion of photons and neutrinos. *Eur. Phys. J. C*, 79(1):44, 2019. [doi:10.1140/epjc/s10052-019-6543-8](https://doi.org/10.1140/epjc/s10052-019-6543-8).
- [17] Tian-Chi Ma, He-Xu Zhang, Peng-Zhang He, Hao-Ran Zhang, Yuan Chen, and Jian-Bo Deng. Shadow cast by a rotating and nonlinear magnetic-charged black hole in perfect fluid dark matter. *Mod. Phys. Lett. A*, 36(17):2150112, 2021. [arXiv:2010.00151](https://arxiv.org/abs/2010.00151), [doi:10.1142/S0217732321501121](https://doi.org/10.1142/S0217732321501121).
- [18] Zezhou Hu, Zhen Zhong, Peng-Cheng Li, Minyong Guo, and Bin Chen. QED effect on a black hole shadow. *Phys. Rev. D*, 103(4):044057, 2021. [arXiv:2012.07022](https://arxiv.org/abs/2012.07022), [doi:10.1103/PhysRevD.103.044057](https://doi.org/10.1103/PhysRevD.103.044057).
- [19] S. I. Kruglov. The shadow of M87* black hole within rational nonlinear electrodynamics. *Mod. Phys. Lett. A*, 35(35):2050291, 2020. [arXiv:2009.07657](https://arxiv.org/abs/2009.07657), [doi:10.1142/S0217732320502910](https://doi.org/10.1142/S0217732320502910).
- [20] Zhen Zhong, Zezhou Hu, Haopeng Yan, Minyong Guo, and Bin Chen. QED effects on Kerr black hole shadows immersed in uniform magnetic fields. *Phys. Rev. D*, 104(10):104028, 2021. [arXiv:2108.06140](https://arxiv.org/abs/2108.06140), [doi:10.1103/PhysRevD.104.104028](https://doi.org/10.1103/PhysRevD.104.104028).
- [21] Aoyun He, Jun Tao, Peng Wang, Yadong Xue, and Ling kai Zhang. Effects of Born-Infeld electrodynamics on black hole shadows. 5 2022. [arXiv:2205.12779](https://arxiv.org/abs/2205.12779). I
- [22] Liang Ma and H. Lu. Bounds on photon spheres and shadows of charged black holes in Einstein–Gauss–Bonnet–Maxwell gravity. *Phys. Lett. B*, 807:135535, 2020. [arXiv:1912.05569](https://arxiv.org/abs/1912.05569), [doi:10.1016/j.physletb.2020.135535](https://doi.org/10.1016/j.physletb.2020.135535). I
- [23] Shao-Wen Wei and Yu-Xiao Liu. Testing the nature of Gauss-Bonnet gravity by four-dimensional rotating black hole shadow. *Eur. Phys. J. Plus*, 136(4):436, 2021. [arXiv:2003.07769](https://arxiv.org/abs/2003.07769), [doi:10.1140/epjp/s13360-021-01398-9](https://doi.org/10.1140/epjp/s13360-021-01398-9).
- [24] Xiao-Xiong Zeng, Hai-Qing Zhang, and Hongbao Zhang. Shadows and photon spheres with spherical accretions in the four-dimensional Gauss–Bonnet black hole. *Eur. Phys. J. C*, 80(9):872, 2020. [arXiv:2004.12074](https://arxiv.org/abs/2004.12074), [doi:10.1140/epjc/s10052-020-08449-y](https://doi.org/10.1140/epjc/s10052-020-08449-y).

- [25] Minyong Guo and Peng-Cheng Li. Innermost stable circular orbit and shadow of the 4D Einstein–Gauss–Bonnet black hole. *Eur. Phys. J. C*, 80(6):588, 2020. [arXiv:2003.02523](#), [doi:10.1140/epjc/s10052-020-8164-7](#). I
- [26] Dmitry Ayzenberg and Nicolas Yunes. Black Hole Shadow as a Test of General Relativity: Quadratic Gravity. *Class. Quant. Grav.*, 35(23):235002, 2018. [arXiv:1807.08422](#), [doi:10.1088/1361-6382/aae87b](#). I
- [27] Leonardo Amarilla, Ernesto F. Eiroa, and Gaston Giribet. Null geodesics and shadow of a rotating black hole in extended Chern-Simons modified gravity. *Phys. Rev. D*, 81:124045, 2010. [arXiv:1005.0607](#), [doi:10.1103/PhysRevD.81.124045](#). I
- [28] Sara Dastan, Reza Saffari, and Saheb Soroushfar. Shadow of a Charged Rotating Black Hole in $f(R)$ Gravity. 6 2016. [arXiv:1606.06994](#). I
- [29] Andrea Addazi, Salvatore Capozziello, and Sergei Odintsov. Chaotic solutions and black hole shadow in $f(R)$ gravity. *Phys. Lett. B*, 816:136257, 2021. [arXiv:2103.16856](#), [doi:10.1016/j.physletb.2021.136257](#).
- [30] Guo-Ping Li and Ke-Jian He. Observational appearances of a $f(R)$ global monopole black hole illuminated by various accretions. *Eur. Phys. J. C*, 81(11):1018, 2021. [doi:10.1140/epjc/s10052-021-09817-y](#). I
- [31] Leonardo Amarilla and Ernesto F. Eiroa. Shadow of a rotating braneworld black hole. *Phys. Rev. D*, 85:064019, 2012. [arXiv:1112.6349](#), [doi:10.1103/PhysRevD.85.064019](#). I
- [32] Minyong Guo, Shupeng Song, and Haopeng Yan. Observational signature of a near-extremal Kerr-Sen black hole in the heterotic string theory. *Phys. Rev. D*, 101(2):024055, 2020. [arXiv:1911.04796](#), [doi:10.1103/PhysRevD.101.024055](#).
- [33] Tao Zhu, Qiang Wu, Mubasher Jamil, and Kimet Jusufi. Shadows and deflection angle of charged and slowly rotating black holes in Einstein-Æther theory. *Phys. Rev. D*, 100(4):044055, 2019. [arXiv:1906.05673](#), [doi:10.1103/PhysRevD.100.044055](#).
- [34] Rahul Kumar, Sushant G. Ghosh, and Anzhong Wang. Gravitational deflection of light and shadow cast by rotating Kalb-Ramond black holes. *Phys. Rev. D*, 101(10):104001, 2020. [arXiv:2001.00460](#), [doi:10.1103/PhysRevD.101.104001](#). I
- [35] Shao-Wen Wei and Yu-Xiao Liu. Observing the shadow of Einstein-Maxwell-Dilaton-Axion black hole. *JCAP*, 11:063, 2013. [arXiv:1311.4251](#), [doi:10.1088/1475-7516/2013/11/063](#). I
- [36] Mingzhi Wang, Songbai Chen, and Jiliang Jing. Shadow casted by a Konoplya-Zhidenko rotating non-Kerr black hole. *JCAP*, 10:051, 2017. [arXiv:1707.09451](#), [doi:10.1088/1475-7516/2017/10/051](#).
- [37] Ming Zhang and Jie Jiang. Shadows of accelerating black holes. *Phys. Rev. D*, 103(2):025005, 2021. [arXiv:2010.12194](#), [doi:10.1103/PhysRevD.103.025005](#).
- [38] Xiao-Xiong Zeng, Ke-Jian He, and Guo-Ping Li. Effect of dark matter on shadows and rings of a brane-world black hole illuminated by various accretions. 11 2021. [arXiv:2111.05090](#).
- [39] Yang Guo and Yan-Gang Miao. Charged black-bounce spacetimes: Photon rings, shadows and obser-

- vational appearances. 12 2021. [arXiv:2112.01747](#).
- [40] Yuan Meng, Xiao-Mei Kuang, and Zi-Yu Tang. Photon regions, shadow observables and constraints from M87* of a charged rotating black hole. 4 2022. [arXiv:2204.00897](#).
- [41] Chen-Kai Qiao and Ming Li. A Geometric Approach on Circular Photon Orbits and Black Hole Shadow. 4 2022. [arXiv:2204.07297](#).
- [42] Igor Bogush, Dmitri Gal'tsov, Galin Gyulchev, Kirill Kobialko, Petya Nedkova, and Tsvetan Vetsov. Photon surfaces, shadows and accretion disks in gravity with minimally coupled scalar field. 5 2022. [arXiv:2205.01919](#).
- [43] Sen Guo, Guan-Ru Li, and En-Wei Liang. Observable characteristics of the charged black hole surrounded by thin disk accretion in Rastall gravity. *Class. Quant. Grav.*, 39(13):135004, 2022. [arXiv:2205.11241](#), [doi:10.1088/1361-6382/ac6fa8](#).
- [44] Hui-Min Wang, Zi-Chao Lin, and Shao-Wen Wei. Optical appearance of Einstein-Æther black hole surrounded by thin disk. 5 2022. [arXiv:2205.13174](#).
- [45] Zelin Zhang, Songbai Chen, and Jiliang Jing. Image of Bonnor black dihole with a thin accretion disk and its polarization information. 5 2022. [arXiv:2205.13696](#).
- [46] Yehui Hou, Peng Liu, Minyong Guo, Haopeng Yan, and Bin Chen. Multi-level images around Kerr-Newman black holes. 3 2022. [arXiv:2203.02755](#). I
- [47] Pedro V. P. Cunha, Emanuele Berti, and Carlos A. R. Herdeiro. Light-Ring Stability for Ultracompact Objects. *Phys. Rev. Lett.*, 119(25):251102, 2017. [arXiv:1708.04211](#), [doi:10.1103/PhysRevLett.119.251102](#). I
- [48] Bakhtiyor Narzilloev, Javlon Rayimbaev, Sanjar Shaymatov, Ahmadjon Abdujabbarov, Bobomurat Ahmedov, and Cosimo Bambi. Can the dynamics of test particles around charged stringy black holes mimic the spin of Kerr black holes? *Phys. Rev. D*, 102(4):044013, 2020. [arXiv:2007.12462](#), [doi:10.1103/PhysRevD.102.044013](#).
- [49] Minyong Guo and Sijie Gao. Universal Properties of Light Rings for Stationary Axisymmetric Spacetimes. *Phys. Rev. D*, 103(10):104031, 2021. [arXiv:2011.02211](#), [doi:10.1103/PhysRevD.103.104031](#).
- [50] Carlos A. R. Herdeiro, Alexandre M. Pombo, Eugen Radu, Pedro V. P. Cunha, and Nicolas Sanchis-Gual. The imitation game: Proca stars that can mimic the Schwarzschild shadow. *JCAP*, 04:051, 2021. [arXiv:2102.01703](#), [doi:10.1088/1475-7516/2021/04/051](#). I
- [51] Vitor Cardoso, Edgardo Franzin, and Paolo Pani. Is the gravitational-wave ringdown a probe of the event horizon? *Phys. Rev. Lett.*, 116(17):171101, 2016. [Erratum: *Phys.Rev.Lett.* 117, 089902 (2016)]. [arXiv:1602.07309](#), [doi:10.1103/PhysRevLett.116.171101](#). I
- [52] Zachary Mark, Aaron Zimmerman, Song Ming Du, and Yanbei Chen. A recipe for echoes from exotic compact objects. *Phys. Rev. D*, 96(8):084002, 2017. [arXiv:1706.06155](#), [doi:10.1103/PhysRevD.96.084002](#).
- [53] Pablo Bueno, Pablo A. Cano, Frederik Goelen, Thomas Hertog, and Bert Vercknocke. Echoes of Kerr-like wormholes. *Phys. Rev. D*, 97(2):024040, 2018. [arXiv:1711.00391](#), [doi:10.1103/PhysRevD.97](#).

- 024040.
- [54] R. A. Konoplya, Z. Stuchlík, and A. Zhidenko. Echoes of compact objects: new physics near the surface and matter at a distance. *Phys. Rev. D*, 99(2):024007, 2019. [arXiv:1810.01295](#), [doi:10.1103/PhysRevD.99.024007](#).
 - [55] Yu-Tong Wang, Jun Zhang, and Yun-Song Piao. Primordial gravastar from inflation. *Phys. Lett. B*, 795:314–318, 2019. [arXiv:1810.04885](#), [doi:10.1016/j.physletb.2019.06.036](#).
 - [56] Yu-Tong Wang, Zhi-Peng Li, Jun Zhang, Shuang-Yong Zhou, and Yun-Song Piao. Are gravitational wave ringdown echoes always equal-interval? *Eur. Phys. J. C*, 78(6):482, 2018. [arXiv:1802.02003](#), [doi:10.1140/epjc/s10052-018-5974-y](#).
 - [57] Vitor Cardoso and Paolo Pani. Testing the nature of dark compact objects: a status report. *Living Rev. Rel.*, 22(1):4, 2019. [arXiv:1904.05363](#), [doi:10.1007/s41114-019-0020-4](#).
 - [58] José T. Gálvez Gherzi, Andrei V. Frolov, and David A. Dobre. Echoes from the scattering of wavepackets on wormholes. *Class. Quant. Grav.*, 36(13):135006, 2019. [arXiv:1901.06625](#), [doi:10.1088/1361-6382/ab23c8](#).
 - [59] Hang Liu, Peng Liu, Yunqi Liu, Bin Wang, and Jian-Pin Wu. Echoes from phantom wormholes. *Phys. Rev. D*, 103(2):024006, 2021. [arXiv:2007.09078](#), [doi:10.1103/PhysRevD.103.024006](#).
 - [60] Yi Yang, Dong Liu, Zhaoyi Xu, Yujia Xing, Shurui Wu, and Zheng-Wen Long. Echoes of novel black-bounce spacetimes. *Phys. Rev. D*, 104(10):104021, 2021. [arXiv:2107.06554](#), [doi:10.1103/PhysRevD.104.104021](#).
 - [61] Min-Yan Ou, Meng-Yun Lai, and Hyat Huang. Echoes from Asymmetric Wormholes and Black Bounce. 11 2021. [arXiv:2111.13890](#). I
 - [62] Xiaobao Wang, Peng-Cheng Li, Cheng-Yong Zhang, and Minyong Guo. Novel shadows from the asymmetric thin-shell wormhole. *Phys. Lett. B*, 811:135930, 2020. [arXiv:2007.03327](#), [doi:10.1016/j.physletb.2020.135930](#). I, II, II
 - [63] Maciek Wielgus, Jiri Horak, Frederic Vincent, and Marek Abramowicz. Reflection-asymmetric wormholes and their double shadows. *Phys. Rev. D*, 102(8):084044, 2020. [arXiv:2008.10130](#), [doi:10.1103/PhysRevD.102.084044](#).
 - [64] Merce Guerrero, Gonzalo J. Olmo, and Diego Rubiera-Garcia. Double shadows of reflection-asymmetric wormholes supported by positive energy thin-shells. *JCAP*, 04:066, 2021. [arXiv:2102.00840](#), [doi:10.1088/1475-7516/2021/04/066](#).
 - [65] Jun Peng, Minyong Guo, and Xing-Hui Feng. Observational signature and additional photon rings of an asymmetric thin-shell wormhole. *Phys. Rev. D*, 104(12):124010, 2021. [arXiv:2102.05488](#), [doi:10.1103/PhysRevD.104.124010](#). II, II
 - [66] Merce Guerrero, Gonzalo J. Olmo, Diego Rubiera-Garcia, and Diego Gómez Sáez-Chillón. Light ring images of double photon spheres in black hole and wormhole spacetimes. *Phys. Rev. D*, 105(8):084057, 2022. [arXiv:2202.03809](#), [doi:10.1103/PhysRevD.105.084057](#). I
 - [67] Carlos A.R. Herdeiro, Eugen Radu, Nicolas Sanchis-Gual, and José A. Font. Spontaneous Scalarization

- of Charged Black Holes. *Phys. Rev. Lett.*, 121(10):101102, 2018. [arXiv:1806.05190](#), [doi:10.1103/PhysRevLett.121.101102](#). I
- [68] Peng Wang, Houwen Wu, and Haitang Yang. Scalarized Einstein-Born-Infeld black holes. *Phys. Rev. D*, 103(10):104012, 2021. [arXiv:2012.01066](#), [doi:10.1103/PhysRevD.103.104012](#).
- [69] Qingyu Gan, Peng Wang, Houwen Wu, and Haitang Yang. Photon spheres and spherical accretion image of a hairy black hole. *Phys. Rev. D*, 104(2):024003, 2021. [arXiv:2104.08703](#), [doi:10.1103/PhysRevD.104.024003](#).
- [70] Guangzhou Guo, Peng Wang, Houwen Wu, and Haitang Yang. Scalarized Einstein–Maxwell-scalar black holes in anti-de Sitter spacetime. *Eur. Phys. J. C*, 81(10):864, 2021. [arXiv:2102.04015](#), [doi:10.1140/epjc/s10052-021-09614-7](#).
- [71] Guangzhou Guo, Peng Wang, Houwen Wu, and Haitang Yang. Thermodynamics and phase structure of an Einstein-Maxwell-scalar model in extended phase space. *Phys. Rev. D*, 105(6):064069, 2022. [arXiv:2107.04467](#), [doi:10.1103/PhysRevD.105.064069](#). I
- [72] Qingyu Gan, Peng Wang, Houwen Wu, and Haitang Yang. Photon ring and observational appearance of a hairy black hole. *Phys. Rev. D*, 104(4):044049, 2021. [arXiv:2105.11770](#), [doi:10.1103/PhysRevD.104.044049](#). I
- [73] Guangzhou Guo, Xin Jiang, Peng Wang, and Houwen Wu. Gravitational Lensing by Black Holes with Multiple Photon Spheres. 4 2022. [arXiv:2204.13948](#). I
- [74] Guangzhou Guo, Peng Wang, Houwen Wu, and Haitang Yang. Quasinormal modes of black holes with multiple photon spheres. *JHEP*, 06:060, 2022. [arXiv:2112.14133](#), [doi:10.1007/JHEP06\(2022\)060](#). I
- [75] Guangzhou Guo, Peng Wang, Houwen Wu, and Haitang Yang. Echoes from hairy black holes. *JHEP*, 06:073, 2022. [arXiv:2204.00982](#), [doi:10.1007/JHEP06\(2022\)073](#). I
- [76] Vitor Cardoso, Francisco Duque, and Arianna Foschi. Light ring and the appearance of matter accreted by black holes. *Phys. Rev. D*, 103(10):104044, 2021. [arXiv:2102.07784](#), [doi:10.1103/PhysRevD.103.104044](#). I, III, III A, IIIB, IIIB, IV
- [77] Yiqian Chen, Guangzhou Guo, Peng Wang, Houwen Wu, and Haitang Yang. Appearance of an Infalling Star in Black Holes with Multiple Photon Spheres. 6 2022. [arXiv:2206.13705](#). I, III A, III A, IV
- [78] Joseph F. Dolan and Daria C Auerswald. A Search for Dying Pulse Trains in Cyg X-1 using RXTE. 4 2011. [arXiv:1104.3164](#). I
- [79] M. Bauböck et al. Modeling the orbital motion of Sgr A*’s near-infrared flares. *Astron. Astrophys.*, 635:A143, 2020. [arXiv:2002.08374](#), [doi:10.1051/0004-6361/201937233](#). I
- [80] R. Abuter et al. The flux distribution of Sgr A*. *Astron. Astrophys.*, 638:A2, 2020. [arXiv:2004.07185](#), [doi:10.1051/0004-6361/202037717](#). I
- [81] Kotaro Moriyama, Shin Mineshige, Mareki Honma, and Kazunori Akiyama. Black hole Spin Measurement Based on Time-domain VLBI Observations of Infalling Gas Cloud. 10 2019. [arXiv:1910.10713](#), [doi:10.3847/1538-4357/ab505b](#). I
- [82] Michael D. Johnson et al. Universal interferometric signatures of a black hole’s photon ring. *Sci. Adv.*,

- 6(12):eaa1310, 2020. [arXiv:1907.04329](#), [doi:10.1126/sciadv.aaz1310](#). I
- [83] Elizabeth Himwich, Michael D. Johnson, Alexandru Lupsasca, and Andrew Strominger. Universal polarimetric signatures of the black hole photon ring. *Phys. Rev. D*, 101(8):084020, 2020. [arXiv:2001.08750](#), [doi:10.1103/PhysRevD.101.084020](#).
- [84] Samuel E. Gralla, Alexandru Lupsasca, and Daniel P. Marrone. The shape of the black hole photon ring: A precise test of strong-field general relativity. *Phys. Rev. D*, 102(12):124004, 2020. [arXiv:2008.03879](#), [doi:10.1103/PhysRevD.102.124004](#). I
- [85] Matt Visser. Traversable wormholes from surgically modified Schwarzschild space-times. *Nucl. Phys. B*, 328:203–212, 1989. [arXiv:0809.0927](#), [doi:10.1016/0550-3213\(89\)90100-4](#). II